Article:
Liu, Y., Zhang, X., Lyu, G. et al. (2022) Effect of the oxidation-induced fragmentation of primary particles on soot oxidation reactivity. Combustion and Flame, 240. 112026. ISSN: 0010-2180

https://doi.org/10.1016/j.combustflame.2022.112026

Effect of the oxidation-induced fragmentation of primary particles on soot oxidation reactivity

Ye Liu [a,b,1], Xuyang Zhang [a,1], Gang Lyu [a], Yuehan Qiao [a], Wei Zhang [a], Chonglin Song [a*]

[a] State Key Laboratory of Engines, Tianjin University, Tianjin 300072, China.

[b] Institute for Transport Studies, University of Leeds, Leeds LS2 9JT, UK.

Abstract: Experiments were performed on a CH_4 lean premixed flame to better understand the effect of the oxidation-induced fragmentation of primary particles on soot oxidation reactivity. An aerosol generator was used to homogeneously disperse diesel soot into the flame. Because minimal soot was formed in this flame itself, the information about diesel soot fragmentation was readily obtained. The thermophoretic and probe sampling techniques were used to obtain soot particles at various heights above the burner. The particle size distribution, oxidation reactivity, nanostructure and carbon chemical state of each sample were characterized. The soot reactivity was evaluated in terms of activation energy. The results indicate a higher extent of aggregate fragmentation occurs at moderate soot burnout percentages and that the internal structure in soot is not destroyed during aggregate fragmentation. At higher soot burnout percentages, the internal burning produces more primary particle fragmentation, so that the soot particles exhibit an increase in fringe tortuosity and decreases in fringe length and sp^2/sp^3 hybridization ratio. These variations in physicochemical properties increase the oxidation reactivity of the soot particles.

Keywords: Soot oxidation; Fragmentation; Primary particle; Oxidation reactivity; Soot property

* Corresponding author. Tel.: +86-22-27406840-8020; fax: +86-22-27403750
Email address: songchonglin@tju.edu.cn (C.-L. Song)
[1] These authors contributed equally to this work.

1. Introduction

Recently, there has been significant interest in the oxidation-induced soot fragmentation because this phenomenon is related not only to soot oxidation but also to soot particle number concentration [1,2]. Neoh et al. [3,4] first reported the evidence of soot fragmentation in a two-stage burner when approximately 70−80% soot was burnt out. They stated that the soot fragmentation led to a noticeable increase in ultrafine particles. Soot fragmentation was also observed by Garo et al. [5], who demonstrated a sharp increase in the number concentration of soot particles as a result. Puri et al. [6] discovered that the fragmentation of soot aggregates increased the number concentration of soot particles in the upstream of a laminar ethylene diffusion flame. Echavarria et al. [7,8] and Ghiassi et al. [9,10] studied the soot fragmentation using a scanning mobility particle sizer. Their experimental results showed a substantial increase in the quantity of the particles smaller than 10 nm following the soot fragmentation in the oxidation region.

A better understanding of soot fragmentation process can also permit optimization of the existing models for predicting the size distribution and number concentration of oxidized soot particles [2,8,10]. Harris et al. [11] reported that the addition of a soot fragmentation event to the Schmoluchowski aerosol coagulation mode greatly increased the prediction of the size distribution. Zhang et al. [12] demonstrated that without taking into account the fragmentation event, the model prediction of soot particle mobility diameter during oxidation was different from the experimental results. Sirignano et al. [13,14] claimed that soot fragmentation had a pronounced effect on the ultimate number concentration of soot particles.

The oxidation-induced soot fragmentation can occur via two mechanisms: aggregate fragmentation and primary particle fragmentation [2,7,9,10]. Aggregate fragmentation results from

the diffusion of oxygen into the regions where primary particles make contact with one another to oxidize the bridges holding the primary particles, thus inducing the breakup of aggregates [2,15,16]. In contrast, during primary particle fragmentation, oxygen diffuses into primary particles to promote internal burning, after which these particles break up into smaller fragments [2,15]. Aggregate fragmentation does not destroy the fringe structure in soot [9,16], whereas primary particle fragmentation inevitably alters the structural properties of soot particles [7,15]. Because soot reactivity strongly depends on its structure [17-20], this structural alteration can affect soot oxidation reactivity.

The sooting process in flames is a complex process during which soot oxidation and formation occur simultaneously. The coexistence of oxidation and formation makes it difficult to explore solely the soot oxidation process, and so there have been few reports related to the effect of the oxidation-induced fragmentation of soot particles on oxidation reactivity. In the present study, diesel soot particles were homogeneously dispersed into CH_4 lean premixed flame via an aerosol generator. Because minimal soot was formed in this flame itself, the information about the oxidation-induced fragmentation of the diesel soot was readily obtained. In addition, the reactivity and structural properties of the diesel soot during oxidation process were examined to assess the effect of primary particle fragmentation on soot reactivity.

2. Experimental

2.1. Burner and sampling system

Figure 1 shows the schematic diagram of the experimental setup. A water-cooled McKenna burner (Holthius and Associates) with a center tube (12.7 mm inner diameter) and a bronze porous plug (75 mm inner diameter) was used in this work. The center tube supplied a $CH_4/O_2/N_2$ gas

65 mixture at a cold flow rate of 65 cm/min to generate a CH_4 lean premixed flame. This same mixture
66 was passed through the external porous plug at a cold flow rate of 4 cm/min to produce a pilot
67 flame that stabilized the central flame. The equivalence ratios of both the center and pilot flames
68 were set at 0.9. Soot collected from diesel engine exhaust and thoroughly ground in an agate mortar
69 was fed into flame by an aerosol generator (Palas RGB-1000-GD), because it can generate solid
70 aerosols steadily at very low feed rate. In the aerosol generator, a rotating brush was used to
71 disperse the soot sample into the $CH_4/O_2/N_2$ stream. During test, a high rotating speed of the brush
72 (1200 rpm) and a small feed rate of the soot (1.5 mg/min) were used to ensure the dispersion
73 homogeneity of the soot. To validate the feasibility of this method, further analysis was carried out
74 using the scanning mobility particle sizer. At HAB = 0 mm, the particle size distributions (PSDs)
75 at the burner center and at a radial location of 3 mm from the burner center were measured before
76 the flame was ignited. It can be seen from Fig. 2 that the PSDs are almost the same at the two
77 measurement points, indicating that the soot particles were homogeneously dispersed into the
78 $CH_4/O_2/N_2$ stream. The burner was mounted on a motorized translation stage with a positional
79 accuracy of ±0.005 mm to allow the sampling location to be adjusted along the axial direction of
80 the flame.

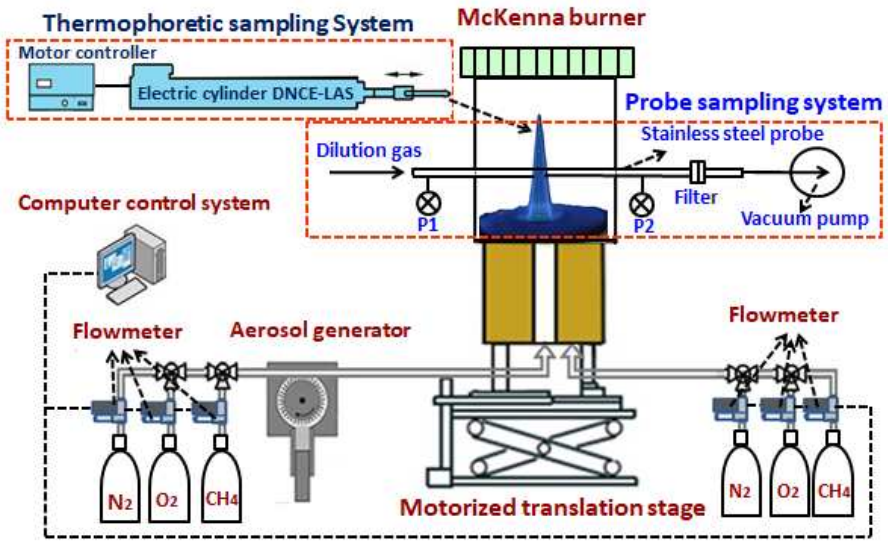

Fig. 1. Schematic diagram of the experimental setup.

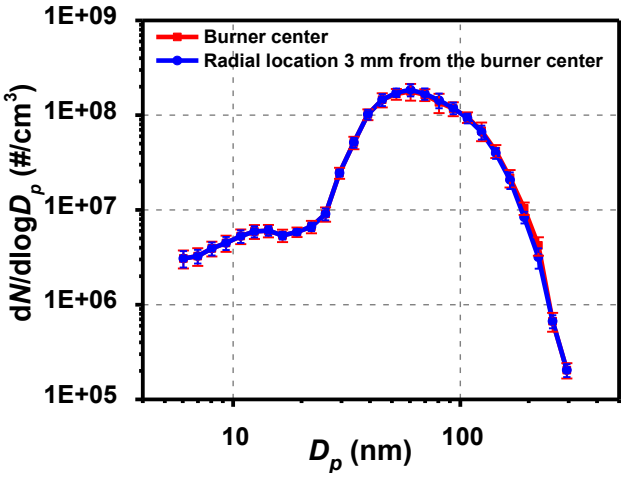

Fig. 2. Particle size distributions (PSDs) at HAB = 0 mm.

The visible flame height was 22 mm, as shown in Fig. 3, and soot samples were collected at a series of height above burner (HAB) values along the axis of the central premixed flame. Details regarding the sampling positions and flame temperatures are provided in Table 1. The flame temperatures along the axial direction were measured using an R-type thermocouple (Pt/Pt−13% Rh) with a 30 μm wire and a bead diameter of approximately 150 μm. The temperatures obtained were corrected for radiative heat loss according to the method reported in [21,22], and the uncertainty in the measurement of flame temperature was determined to be less than ±50 K. The temperature measurement process was elaborated in the Supplementary material.

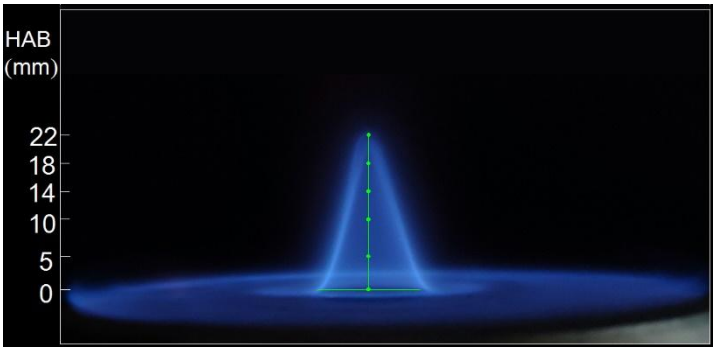

Fig. 3. A photographic image of the flame with soot addition during the experimental trials.

Table 1 Experimental sampling conditions

Sampling positions HAB(mm)	4	8	12	14	16	18	22
Flame temperature at sampling position (K)	1644	1607	1586	1574	1561	1537	1490

Both thermophoretic and probe sampling systems were used to acquire the soot particles at various HABs. The thermophoretic sampling system included an advanced linear electric cylinder (FESTO, Germany) capable of rapid and precise reciprocating motion with an acceleration and speed of 120 m/s^2 and 3 m/s, respectively, and the relative residence time of sampling soot particles was 30 ms. A self-closing tweezer (N5, Switzerland) was mounted on the piston rod to conveniently fix and detach the C/Cu grid that was used to collect soot particles. The probe sampling system was used to obtain sufficient soot for further analysis. The probe in this system had a diameter of 3.175 mm and a wall thickness of 0.125 mm and was placed horizontally above the burner. The probe had a 0.15 mm sampling orifice that faced downward toward the incoming combustion gases and was connected to a vacuum pump that assisted in the collection of soot particles onto a Teflon filter. Nitrogen was supplied during the sampling process at 29.6 L/min to quench the chemical reactions of the flame gases as they were drawn into the sampling tube [23]. To avoid clogging the sampling orifice of the probe sample system, the time for the sampling

procedure was set to 3 min. For each sampling point, the sampling procedure was repeated 5-20 times, depending on the HAB.

2.2. Soot characterization

2.2.1. Scanning mobility particle sizer (SMPS)

The PSDs over the range from 5.6 to 560 nm as well as particle number concentrations were determined using an SMPS (TSI 3090) at a 10Hz data collection frequency. The SMPS sampling system is similar to that of Zhao et al. [23]. The dilution ratio ranged from 10^2 to 10^3 to quench the chemical reactions and minimize soot particle coagulation and losses in the sampling tube [8,23]. The diffusion coagulation and losses along the sampling tube were corrected based on the procedure proposed by Minutolo et al. [24]. Based on the SMPS sizes and particle number concentrations, the soot mass concentrations were calculated according to the method in [25-27]. Detailed calculation process was provided in the Supplementary material.

2.2.2. Thermogravimetric (TG) analysis

The soot reactivity was assessed by non-isothermal TG tests using a TG analyzer (Mettler-Toledo TGA/DSC1). Prior to each experiment, the soot sample was heated at 500 ºC under a 60 ml/min nitrogen flow for 60 min to drive off volatile compounds. Subsequently, the temperature was reduced to 200 ºC, and the sample was then heated at 5 ºC /min to 800 ºC in a 60 ml/min flow of ultrahigh purity air. The TG test was repeated three times for each soot sample to calculate the experimental uncertainty.

2.2.3. High-resolution transmission electron microscopy (HRTEM)

HRTEM (JEOL EM-2010F) with a point resolution of 0.248 nm operating at 200 kV was employed to obtain soot morphology and HRTEM images at a magnification of 40,000× and

400,000×, respectively. The HRTEM images obtained were digitized, and a lattice fringe analysis was performed using an automated fringe image processing system to quantitatively assess the nanostructure parameters, including the fringe length (the graphene layer dimension) and tortuosity (the ratio of the actual fringe length to the straight-line distance). This fringe image processing system involved separate steps of image normalization, region of interest selection, segmentation, enhancement, Gaussian lowpass filter, binary image conversion, skeletonization, post-processing and quantitative analysis of nanostructure parameters. Fringe length was calculated by counting the number of pixels along a fringe and computing the length using a calibrated pixel size. Fringe tortuosity was obtained by calculating the ratio of the fringe length to the straight-line distance between the endpoints of the fringe. More details on the determination of the nanostructure parameters were reported by Yehliu et al. [28].

2.2.4. X-ray diffraction (XRD)

The crystallite parameters of the soot particles were evaluated using a Rigaku D/MAC/max 2500v/pc powder XRD with Cu Kα radiation (40 kV, 200 mA, λ = 1.5406 Å). In preparation for analysis, soot particles were pressed into a groove in a quartz block. A scan range of 5°–110° was used with a scan step size of 0.02° and a scan speed of 10 s/step. A silicon standard was employed to correct diffraction peaks broadening as a result of various instrumental factors.

2.2.5. X-ray photoelectron spectroscopy (XPS)

The carbon chemical state of soot samples was determined using XPS. XPS spectra were recorded by a PerkinElmer PHI-1600 ESCA spectrometer using an Mg Ka X-ray source. The binding energies were calibrated using the C1s peak of contaminant carbon at a binding energy of 284.6 eV as an internal standard. XPS data from three different sections of the soot particles were

averaged, and the uncertainty was less than 6%.

3. Results and discussion

3.1. Oxidation-induced soot fragmentation

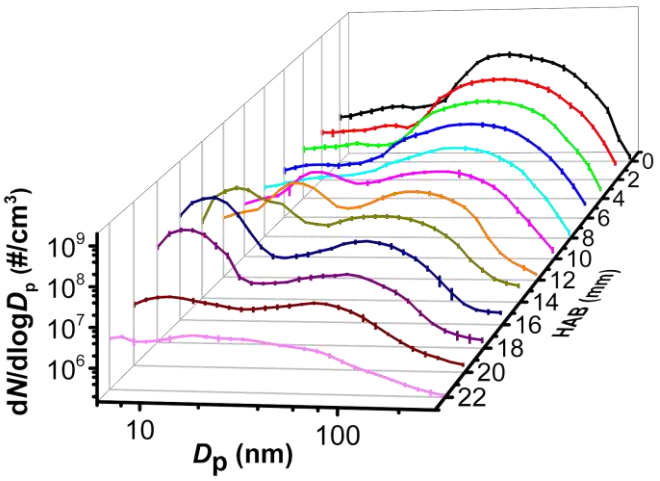

Fig. 4. Particle size distributions (PSDs) as functions of the height above the burner (HAB). The error bars indicate the standard error.

The PSDs of the soot samples were used to characterize the soot oxidation behaviors. According to the proposal by Desantes et al. [29], the soot particles with mobility diameter (D_p)≤ 30 nm are defined as the nucleation mode, while those with D_p > 30 nm are defined as accumulation mode. Figure 4 shows the PSDs at various HABs. In the HAB range of 0−8 mm, the PSDs are unimodal and are dominated almost entirely by the accumulation mode particles. As the HAB increases from 8 to 18 mm, large numbers of nucleation mode particles are formed so that the PSDs gradually become bimodal. In the upper regions of the flame, the number concentrations of both nucleation and accumulation mode particles slowly decrease with increases in the HAB, and the majority of the soot particles are burnt out at HAB = 22 mm. To assess whether the particles generated by the CH_4 combustion in the flame have an effect on the PSDs, the integrated number concentrations of the particles in the flames with and without soot addition are calculated and shown in Fig. 5. It is obvious that the integrated number concentrations for both nucleation and

accumulation mode particles in the flame with soot addition are approximately 3−5 orders of magnitude higher than those without soot addition. Thus, the particles generated from the flame itself can be considered negligible in this analysis.

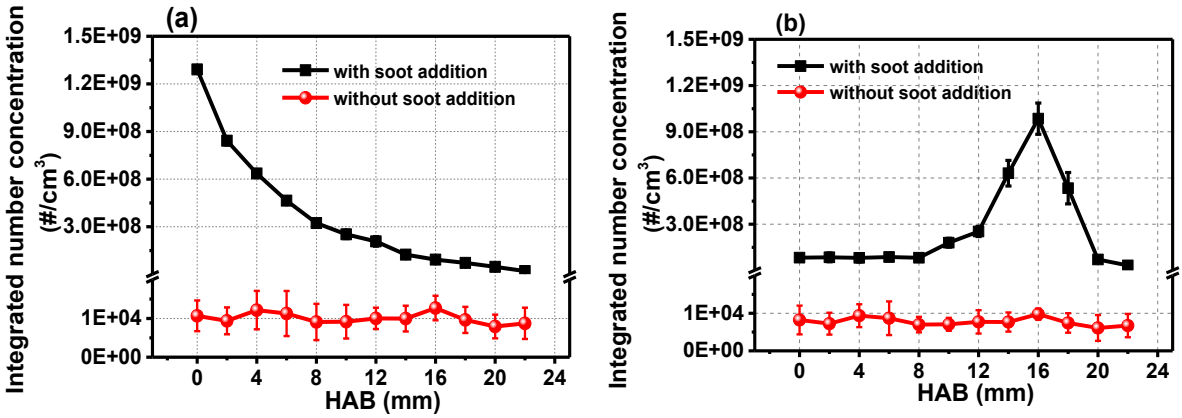

Fig. 5. Integrated number concentrations at various heights above the burner (HABs) for (a) accumulation and (b) nucleation mode particles. The error bars indicate the standard error.

Figure 5 also demonstrates that the integrated number concentrations of accumulation mode particles decrease with increases in the HAB, due to the elimination of many accumulation mode particles by partial and/or complete oxidation. However, the integrated number concentrations of nucleation mode particles plateau and remain relatively constant in the HAB range of 0−8 mm. This phenomenon suggests that a certain extent of soot fragmentation has already taken place in the lower regions of the flame, which compensates for the reduction in the quantity of nucleation mode particles caused by soot oxidation. As the HAB increases from 8 to 16 mm, the significant increase in the number concentrations of nucleation mode particles indicates the occurrence of a high extent of soot fragmentation. With further increases in the HAB, the number concentrations of nucleation mode particles show a sharp decrease as a consequence of the soot burnout and the reduction in soot fragmentation. Ghiassi et al. [9,30] and Sirignano et al. [2] pointed out that the concentration of ultrafine particle (D_p<10 nm) was associated with the fragmentation of the primary particles. On this basis, the present work uses the ultrafine particle concentration to

estimate the extent of primary particle fragmentation. Figure 6 shows the integrated number concentrations of ultrafine particles, overall soot mass concentrations and the overall soot burnout percentages at various HABs. It is seen that when the HAB increases from 12 to 16 mm (corresponding to 68–87% soot burnout), the soot fragmentation results in a nearly 22-fold increase in the number concentration, despite a significant reduction of overall soot mass concentration. The present results are in agreement with prior reports by Neoh et al. [3,4] and Garo et al. [5], who revealed the presence of ultrafine particles at 70–80% soot burnout. They attributed this behavior to the fragmentation or breakup of primary particles caused by internal burning.

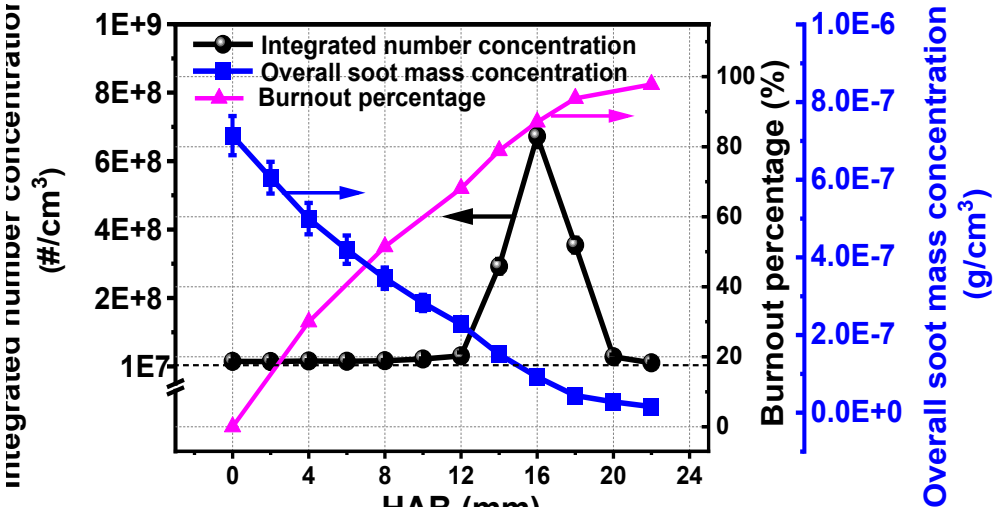

Fig. 6. Integrated number concentrations of ultrafine particles (D_p<10 nm), overall soot mass concentrations and overall soot burnout percentages at various heights above the burner (HABs). The error bars indicate the standard error.

To examine the possibility that numerous ultrafine particles are generated as a consequence of internal burning, the primary particle diameters with oxidation are calculated and shown in Fig. 7. Also, the theoretical models for constant diameter burning and constant density burning (or external/shrinking burning) are shown in Fig. 7. The constant density burning can be expressed as [17]:

$$\frac{d(X)}{d_0} = (1 - X)^{1/3} \quad (1)$$

where d_0, $d(X)$, and X are the initial particle diameter, the particle diameter at a given conversion level, and the conversion level, respectively. Ishiguro et al. [31] examined the microstructural changes of diesel soot during oxidation, and their data can be fitted with good accuracy using the following equation [32]:

$$\frac{d(X)}{d_0} = (1 - X)^{1/6} \quad (2)$$

Eq. (2) is the reference condition under which the contributions of internal and external burning to the total oxidized soot mass are comparable [1,32]. For comparison purposes, Eq. (2) is also presented in Fig. 7. It is seen that at HAB < 12 mm, the soot particles lie in the region where external burning is dominant. However, as the HAB increases from 12 mm to 16 mm, the soot particles shift toward the region where internal burning is dominant. In addition, it is interesting to note that no noticeable variation in d/d_0 is identified from HAB = 12 mm to 16 mm although the corresponding burnout percentages increase from 68.1% to 87.1%, suggesting a great extent of internal burning within this range of HABs. From the results above, it can be inferred that the internal burning is responsible for the appearance of ultrafine particles at high burnout percentages. Moreover, the HRTEM analysis of soot particles was carried out to provide additional evidence for the occurrence of internal burning. The examples of HRTEM images of soot particles at different HABs are given in Fig. S2 of the Supplementary material. At HAB =14 and 16 mm, a substantial quantity of soot particles are readily identified to have hollow interiors with thicker boundaries, as shown in Fig. 8, In addition, typical HRTEM images of the pristine soot are shown in Fig. 9. The absence of hollow structure in the pristine soot affirms that the hollow structure observed in Fig. 8 is formed during soot oxidation process. Previous studies [15,17,33,34] confirmed that such hollow capsule structure for soot particles was a result of internal burning. The above results testify the

occurrence of primary particle fragmentation in this flame. The effects of this fragmentation on the reactivity and properties of soot particles will be discussed in the following sections.

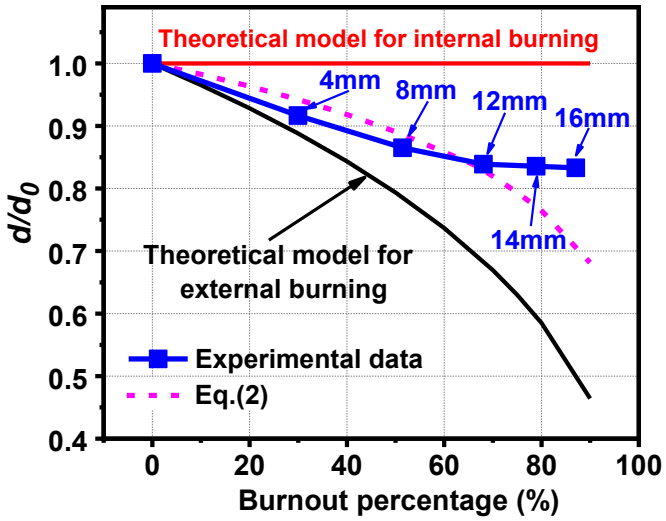

Fig. 7. Reduction in soot particle diameters during the oxidation of soot particles.

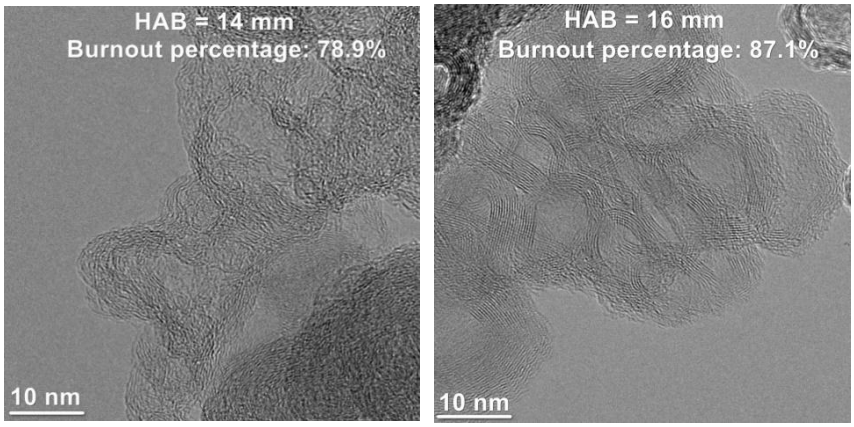

Fig. 8. HRTEM images of the soot particles with hollow capsule structure.

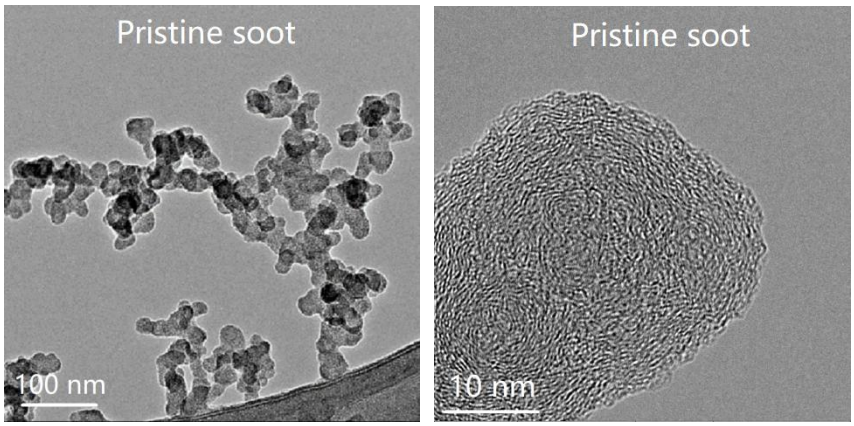

Fig. 9. Typical HRTEM images of the pristine soot.

239

240 *3.2. Soot oxidation reactivity*

241 The soot oxidation reactivity was assessed in terms of the apparent activation energy (E_a). A
242 high E_a indicates low oxidation reactivity and vice versa. E_a was obtained according to the
243 Arrhenius equation:

244 $$-\frac{dm}{dt} = k \cdot m^n = Ae^{-\frac{Ea}{RT}} m^n \quad (3)$$

245 where *m, t, k*, *T* and *A* are the real time sample mass that is undergoing reaction, the reaction time,
246 the reaction rate constant, the absolute temperature of the sample and the frequency factor,
247 respectively. The variable *n* is the reaction order and an assumption of *n*=1 was made in this study
248 [35,36].

249 Figure 10 shows the E_a as a function of the HAB. When the HAB increases from 4 to 12 mm,
250 the increased E_a suggests that the soot particles have a decrease in oxidation reactivity. In the range
251 of HAB from 12 to 16 mm, the soot particles exhibit a sharp decrease in E_a, indicating an increase
252 in soot reactivity. With further increases in the HAB, the increased E_a manifests a decrease in soot
253 oxidation reactivity. Comparing Figs. 6 and 10 suggests that this unexpected increase in soot
254 reactivity is closely related to the formation of ultrafine particles.

255 In Section 3.1, these ultrafine particles were shown to result from the internal burning.
256 Previous studies confirmed that the internal burning could change soot structure. For instance,
257 Song et al. [37] examined the oxidation behavior of the soot generated from neat biodiesel, and
258 found that following the removal of the inner core through internal burning, the soot structure
259 tended to rearrange and coalesce to form a ribbon-like morphology with much flatter and longer
260 layers. Al-Qurashi and Boehman [17] reported that the diesel soot generated from 20% exhaust gas
261 recirculation exhibited dual burning modes with oxidation: external burning and internal burning,

and the internal burning resulted in an increase in interlayer spacing. Given that soot reactivity depends on soot properties, the increased soot reactivity reflected in Fig. 10 suggests that the internal burning results in soot particles with different properties that enhance reactivity.

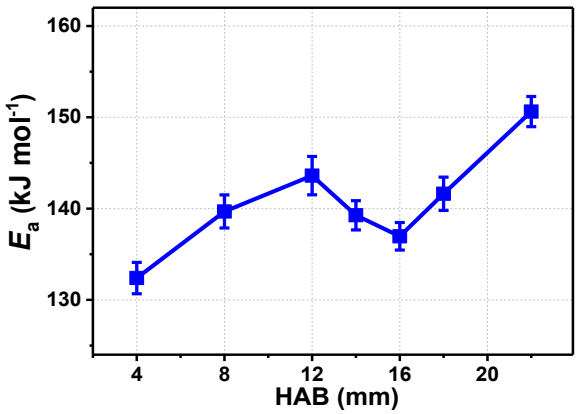

Fig. 10. Activation energy (E_a) as a function of the height above the burner (HAB). The error bars indicate the standard error.

3.3. Soot property

HRTEM was used to evaluate the nanostructural parameters of soot particles, including fringe length and tortuosity. For each sample, more than 150 primary soot particles from different aggregates were randomly selected for these assessments to ensure statistical significance. The average values of fringe length (L_f) and tortuosity (T_f) are plotted against HAB in Fig. 11. A gradual increase in L_f and a decrease in T_f are observed in the HAB range of 4–12 mm, suggesting that the soot evolves towards a better graphitic organization. Such structural evolution is closely associated with the following processes: (1) high-temperature flame environment promotes preferential oxidation of the outermost short and amorphous carbon layers [37]; (2) crystallites grow via the incorporation of existing graphene layers and non-organized carbon, and the wavy layers become much flatter and longer after rearrangement and coalescence of the crystallite layers [37,38]. Previous studies confirmed that the edge carbon atoms in soot had a higher affinity to form bonds with chemisorbed oxygen due to the availability of unpaired sp^2 electrons, while the carbon atoms

281 in the basal planes formed chemical bonds with adjacent carbon atoms based on shared π electrons
282 [39-41]. The carbon atoms at the edges of the graphene sheets were reported to be 100–1000 times
283 more reactive than those in the basal plane [39]. A large L_f value for soot structure corresponds to
284 a lower ratio of edge-to-basal carbon atoms, and thereby is associated with lower reactivity. In
285 addition, a small T_f reflects presence of fewer odd-membered rings or sp^3 hybridized carbon atoms
286 in soot, both of which are more reactive toward oxidation than hexagonal rings containing only sp^2
287 hybridized carbon atoms [19,42,43]. Thus, the soot shows a decreased reactivity in the HAB range
288 of 4–12 mm, as manifested by the increased E_a values in Fig. 10.

289 As the HAB increases further from 12 to 16 mm, the L_f values decrease while the T_f values
290 increase. These unusual changes in L_f and T_f can be ascribed to the fragmentation of primary
291 particles. During the fragmentation process, the lamella inevitably break up such that the fringe
292 length is shortened [44]. Because the fringes with smaller radii have commensurately higher bond
293 strain, there is a corresponding increase in fringe tortuosity [45]. As mentioned above, the decrease
294 in L_a and increase in T_f enhance the soot reactivity, and thus the E_a values in Fig. 10 show a decrease
295 from HAB = 12 to 16 mm. In the HAB range from 16 to 22 mm, the fragments of primary particles
296 (i.e. the ultrafine particles) with shorter fringe length and higher tortuosity are burnt out more
297 rapidly, leading to an increase in L_f and a decrease in T_f as shown in Fig. 11.

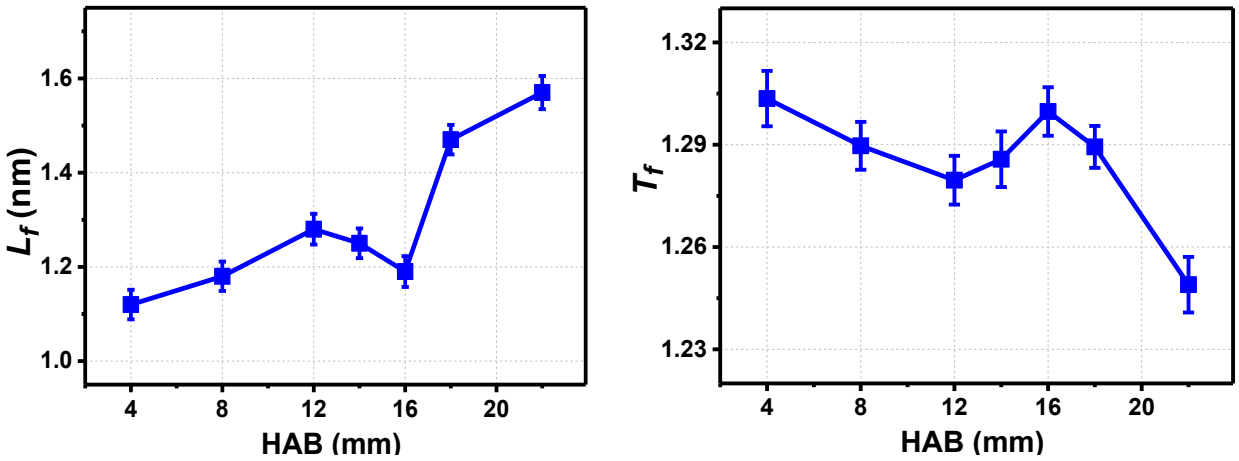

Fig. 11. Mean fringe length (L_f) and tortuosity (T_f) as functions of HAB. The error bars indicate the standard error.

To validate the results of HRTEM analysis, the crystallite width (L_a) for soot particles was determined using XRD. The XRD patterns were fitted using a Gaussian function to obtain the full width at half maximum (FWHM), and the angles of (100) and (002) peaks were determined using the method in [46,47]. The L_a was calculated from the position of the (100) peak using the Scherrer formula:

$$L_a = \frac{K_a \lambda}{B_{100} \cos \theta_{100}} \tag{4}$$

where K_a is a constant with a value of 1.84, λ is the wavelength, θ_{002} and θ_{100} are the Bragg's angles, and B_{100} is the FWHM for the (100) peak. Gaussian curves were fitted to the (002) and (100) peaks to obtain the Bragg's angles and FWHM using Origin 9.0 software.

Figure 12 shows the L_a values obtained from the XRD data of the soot samples at various HABs. The L_a and L_f have a strong linear correlation, as indicated in Fig. S3 of the Supplementary material. Comparing Figs. 11 and 12 highlights that the results obtained from both XRD and HRTEM analyses show similar trends when increasing the HAB. Such a similarity confirms the validity of the HRTEM analysis. Close inspection of Figs. 11 and 12 shows that there is a difference in the data obtained from XRD and HRTEM. This phenomenon has already been addressed in

316 several studies [20,43,47,48]. The peak intensity in the XRD pattern is sensitive to large crystallites.
317 Even though the soot contains a small proportion of large crystallites, they may have a large
318 contribution to the peak intensity. Consequently, XRD is likely to overestimate the crystallite size
319 [47,48]. On the other hand, HRTEM provides images that are essentially two-dimensional
320 projections of three-dimensional soot particles. The quantitative analysis of these images may not
321 give entirely accurate results [20,47]

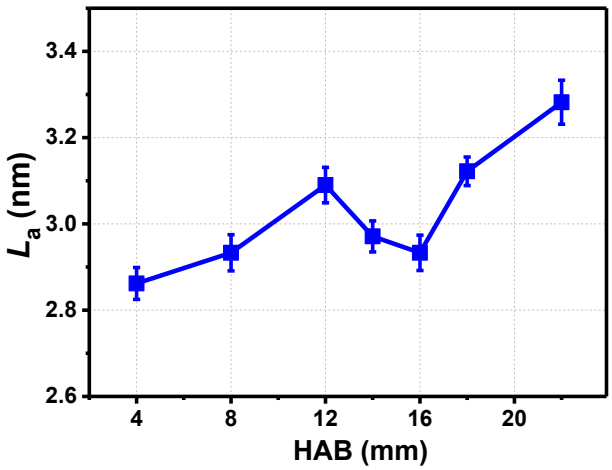

322
323 **Fig. 12.** Crystallite width (L_a) as functions of HAB. The error bars indicate the standard error.

324 The chemical state of the carbon in soot samples was characterized using XPS, and the narrow
325 scan of C1s peak for the soot sample is shown in Fig. 13. To quantify the relative content of sp^2
326 and sp^3 hybridized carbon atoms, the C 1s peaks at 284.6 eV were deconvolved according to the
327 method proposed in [49-51]: the sp^2 hybridized carbon at 284.4 eV, and the sp^3 hybridized carbon
328 at 285.3 eV. The sp^2 hybridized carbon atom corresponds to graphitic carbon within the basal
329 planes, whereas the sp^3 hybridized carbon atom is a class of defects that can disrupt the sp^2
330 hybridized network and require bond terminations other than adjacent π-bonded carbon atoms.
331 These sp^3 carbon atoms reduce the long-range order and are considered to represent defect sites
332 [49,52]. Thus, a lower sp^2/sp^3 ratio indicates a more amorphous structure in the soot [53]. Figure

14 plots the sp^2/sp^3 hybridization ratio as a function of the HAB. The ratio is seen to increase in the HAB range of 4−12 mm, because of crystallite growth and preferential oxidation. That is, the preferential oxidation of amorphous and disordered carbon layers reduces the proportion of sp^3 hybridized carbon [54], while crystallite growth enhances the amount of sp^2 hybridized carbon [54,55]. The sp^2/sp^3 ratio is reduced upon increasing the HAB from 12 to 16 mm. This phenomenon is closely associated with the fragmentation of primary particles because the breakup of lamella in the soot tends to increase the number of sp^3 hybridized carbon atoms while decreasing the fraction of sp^2 hybridized carbon atoms [53]. As the HAB further increases from 16 to 22 mm, the rapid burnout of the primary particle fragments increases the sp^2/sp^3 ratio.

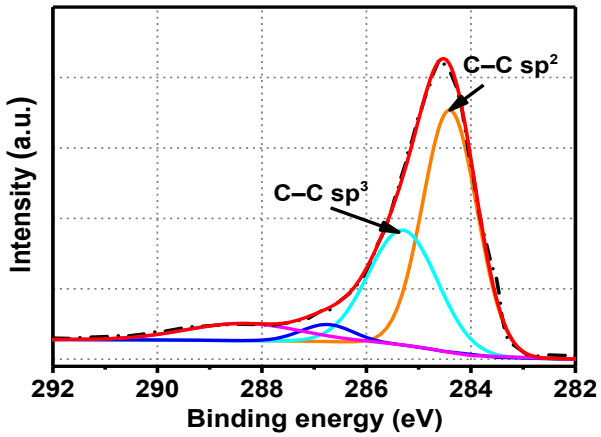

Fig. 13. Typical XPS C 1s narrow spectra for a soot sample.

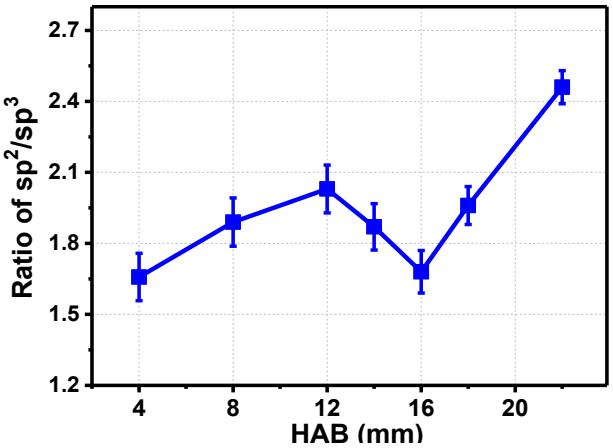

Fig. 14. Ratio of sp^2/sp^3 hybridization as a function of the HAB. The error bars indicate the standard error.

3.4. Perspective on the aggregate fragmentation

The results of the present work indicate that a high extent of primary particle fragmentation occurs in the HAB range of 12−16 mm, and as a consequence, generates numerous ultrafine particles. However, it can be seen from Fig. 5 that there is still an observable increase in the number concentrations of nucleation mode particles in the HAB range of 8−12 mm. Because the number concentration of ultrafine particles (D_p<10 nm) remains relatively constant in this HAB range (see Fig. 6), it is apparent that this increase in the number concentration can be attributed to the formation of the soot particles with 10 <D_p<30 nm. Figure 15 shows the integrated number concentrations of these soot particles and the overall soot burnout percentages at various HABs. It is obvious that there is a significant increase in the integrated number concentration when the HAB increases from 8 to 14 mm, which suggests the occurrence of soot fragmentation.

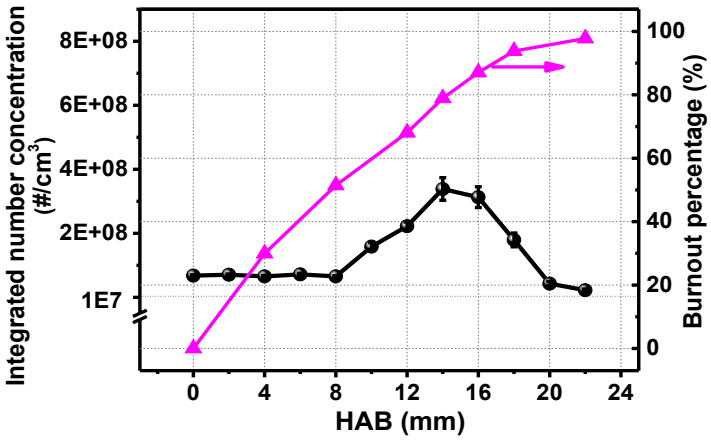

Fig. 15. Integrated number concentrations of the particles with 10 <D_p< 30 nm and the overall soot burnout percentages at various heights above the burner (HABs). The error bars indicate the standard error.

In contrast to the aforementioned primary particle fragmentation, this fragmentation takes place at moderate burnout percentages in the vicinity of 50%. Furthermore, the size of the resulting soot particles is much larger than that of the ultrafine particles resulting from primary particle fragmentation. These differences infer that this process occurs via aggregate fragmentation rather

than primary particle fragmentation. Close inspection of Fig. 15 shows that the number concentration is increased by a factor of 3.4 when increasing the HAB from 8 to 12 mm, reflecting a higher extent of soot fragmentation. However, the shapes of the L_f, T_f and sp^2/sp^3 ratio profiles do not change in this range of HAB, as shown in Figs. 11 and 14, indicating that this fragmentation has no impact on soot structure. Given that aggregate fragmentation does not destroy the internal structure in soot [16], these results can also provide evidence to support the conjecture above. In addition, Figs. 11 and 14 show that there are strong variations in soot structure at HAB > 12 mm, where the aggregate fragmentation still proceeds. It should be noted that this structural variation is not caused by aggregate fragmentation but rather by primary particle fragmentation.

4. Conclusions

In this study, diesel soot was homogeneously dispersed into a CH_4 lean premixed flame to explore the soot oxidation-induced fragmentation and the effect of primary particle fragmentation on soot reactivity. During soot oxidation process, soot fragmentation is dominated by two mechanisms, that is, fragmentation of aggregates and fragmentation of primary particles. A higher extent of aggregate fragmentation takes place at moderate soot burnout percentages (~50%), and as a consequence, increases the number concentration of the soot particles with $10 < D_p < 30$ nm. The aggregate fragmentation has little impact on soot structure and reactivity.

At higher soot burnout percentages (~68−87%), a substantial quantity of soot particles have hollow interiors with thicker boundaries, which is attributed to O_2 penetrating the soot nanostructure and causing internal burning. The internal burning induces the occurrence of primary particle fragmentation, and as a consequence, a great number of ultrafine particles (D_p<10 nm) are generated. In addition, the fragmentation of primary particles decreases the fringe length and

sp^2/sp^3 hybridization ratio, and increase the fringe tortuosity in soot structure. Such structural variations enhance soot reactivity. As the primary particle fragments (i.e., the ultrafine particles) burn out, the soot particles exhibit a decrease in oxidation reactivity, together with increases in fringe length and sp^2/sp^3 hybridization ratio and a decrease in fringe tortuosity.

Acknowledgements

This study was supported by the National Natural Science Foundation of China (91741127), the Science and Technology Research Program of Tianjin (18PTZWHZ00170) and the State Key Laboratory of Engines (K2021-05).

References

[1] G.A. Kelesidis, S.E. Pratsinis, Estimating the internal and surface oxidation of soot agglomerates, Combustion and Flame 209 (2019) 493-499.
[2] M. Sirignano, H. Ghiassi, A. D'Anna, J.S. Lighty, Temperature and oxygen effects on oxidation-induced fragmentation of soot particles, Combustion and Flame 171 (2016) 15-26.
[3] K. G. Neoh, J.B. Howard, A.F. Sarofim, Effect of oxidation on the physical structure of soot, Symposium (International) on Combustion, (1985) 951-957.
[4] K. Neoh, J. Howard, A. Sarofim, Soot oxidation in flames, Particulate Carbon, Springer1981, pp. 261-282.
[5] A. Garo, J. Lahaye, G. Prado, Mechanisms of formation and destruction of soot particles in a laminar methane-air diffusion flame, Proceedings of the Combustion Institute 21 (1988) 1023-1031.
[6] R. Puri, T. Richardson, R. Santoro, R. Dobbins, Aerosol dynamic processes of soot aggregates in a laminar ethene diffusion flame, Combustion and Flame 92 (1993) 320-333.
[7] C.A. Echavarria, I.C. Jaramillo, A.F. Sarofim, J.S. Lighty, Burnout of soot particles in a two-stage burner with a JP-8 surrogate fuel, Combustion and Flame 159 (2012) 2441-2448.
[8] C.A. Echavarria, I.C. Jaramillo, A.F. Sarofim, J.S. Lighty, Studies of soot oxidation and fragmentation in a two-stage burner under fuel-lean and fuel-rich conditions, Proceedings of the Combustion Institute 33 (2011) 659-666.
[9] H. Ghiassi, P. Toth, I.C. Jaramillo, J.S. Lighty, Soot oxidation-induced fragmentation: Part 1: The relationship between soot nanostructure and oxidation-induced fragmentation, Combustion and Flame 163 (2016) 179-187.
[10] H. Ghiassi, I.C. Jaramillo, P. Toth, J.S. Lighty, Soot oxidation-induced fragmentation: Part 2: Experimental investigation of the mechanism of fragmentation, Combustion and Flame 163 (2016) 170-178.
[11] S.J. Harris, M.M. Maricq, The role of fragmentation in defining the signature size distribution of diesel soot, Journal of Aerosol Science 33 (2002) 935-942.

[12] Q. Zhang, M.J. Thomson, H. Guo, F. Liu, G.J. Smallwood, Modeling of oxidation-driven soot aggregate fragmentation in a laminar coflow diffusion flame, Combustion Science and Technology 182 (2010) 491-504.
[13] M. Sirignano, J. Kent, A. D'Anna, Further experimental and modelling evidences of soot fragmentation in flames, Proceedings of the Combustion Institute 35 (2015) 1779-1786.
[14] M. Sirignano, J. Kent, A. D'Anna, Modeling Formation and Oxidation of Soot in Nonpremixed Flames, Energy & Fuels 27 (2013) 2303-2315.
[15] P. Toth, D. Jacobsson, M. Ek, H. Wiinikka, Real-time, in situ, atomic scale observation of soot oxidation, Carbon 145 (2019) 149-160.
[16] A.D. Sediako, C. Soong, J.Y. Howe, M.R. Kholghy, M.J. Thomson, Real-time observation of soot aggregate oxidation in an Environmental Transmission Electron Microscope, Proceedings of the Combustion Institute 36 (2017) 841-851.
[17] K. Al-Qurashi, A.L. Boehman, Impact of exhaust gas recirculation (EGR) on the oxidative reactivity of diesel engine soot, Combustion and Flame 155 (2008) 675-695.
[18] M. Lapuerta, F.J. Martos, J.M. Herreros, Effect of engine operating conditions on the size of primary particles composing diesel soot agglomerates, Journal of Aerosol Science 38 (2007) 455-466.
[19] Z. Li, C. Song, J. Song, G. Lv, S. Dong, Z. Zhao, Evolution of the nanostructure, fractal dimension and size of in-cylinder soot during diesel combustion process, Combustion and Flame 158 (2011) 1624-1630.
[20] M. Lapuerta, J. Rodríguez–Fernández, J. Sánchez-Valdepeñas, Soot reactivity analysis and implications on diesel filter regeneration, Progress in Energy and Combustion Science 78 (2020) 100833.
[21] C.S. McEnally, Ü.Ö. Köylü, L.D. Pfefferle, D.E. Rosner, Soot volume fraction and temperature measurements in laminar nonpremixed flames using thermocouples, Combustion and Flame 109 (1997) 701-720.
[22] M.R. Kholghy, Y. Afarin, A.D. Sediako, J. Barba, M. Lapuerta, C. Chu, J. Weingarten, B. Borshanpour, V. Chernov, M.J. Thomson, Comparison of multiple diagnostic techniques to study soot formation and morphology in a diffusion flame, Combustion and Flame 176 (2017) 567-583.
[23] B. Zhao, Z. Yang, J. Wang, M.V. Johnston, H. Wang, Analysis of soot nanoparticles in a laminar premixed ethylene flame by scanning mobility particle sizer, Aerosol Science and Technology 37 (2003) 611-620.
[24] P. Minutolo, A. D'Anna, A. D'Alessio, On detection of nanoparticles below the sooting threshold, Combustion and Flame 152 (2008) 287-292.
[25] H. Ghiassi, P. Toth, J.S. Lighty, Sooting behaviors of n-butanol and n-dodecane blends, Combustion and Flame 161 (2014) 671-679.
[26] O. Nosko, U. Olofsson, Effective density of airborne wear particles from car brake materials, Journal of Aerosol Science 107 (2017) 94-106.
[27] T. Tzamkiozis, L. Ntziachristos, A. Mamakos, G. Fontaras, Z. Samaras, Aerodynamic and Mobility Size Distribution Measurements to Reveal Biodiesel Effects on Diesel Exhaust Aerosol, Aerosol Science and Technology 45 (2011) 587-595.
[28] K. Yehliu, R.L. Vander Wal, A.L. Boehman, Development of an HRTEM image analysis method to quantify carbon nanostructure, Combustion and Flame 158 (2011) 1837-1851.
[29] J. Desantes, V. Bermudez, A. Garcia, W. Linares, C. Kolodziej, An investigation of particle

size distributions with post injection in DI diesel engines, SAE International, 2011.
[30] H. Ghiassi, Soot oxidation and the mechanisms of oxidation-induced fragmentation in a two-stage burner fro ethylene and surrogate fuels, Ph.D thesis, The University of Utah, (2015).
[31] T. Ishiguro, N. Suzuki, Y. Fujitani, H. Morimoto, Microstructural changes of diesel soot during oxidation, Combustion and Flame 85 (1991) 1-6.
[32] B.R. Stanmore, J.F. Brilhac, P. Gilot, The oxidation of soot: a review of experiments, mechanisms and models, Carbon 39 (2001) 2247-2268.
[33] J. Song, M. Alam, A. Boehman, U. Kim, Examination of the oxidation behavior of biodiesel soot, Combustion and Flame 146 (2006) 589-604.
[34] H.J. Seong, A.L. Boehman, Impact of Intake Oxygen Enrichment on Oxidative Reactivity and Properties of Diesel Soot, Energy & Fuels 25 (2011) 602-616.
[35] D. Zhang, Y. Ma, M. Zhu, Nanostructure and oxidative properties of soot from a compression ignition engine: The effect of a homogeneous combustion catalyst, Proceedings of the Combustion Institute 34 (2013) 1869-1876.
[36] Y. Liu, C. Song, G. Lv, X. Wang, N. Li, Virgin and Extracted Soots in Premixed Methane Flames: A Comparison of Surface Functional Groups, Graphitization Degree, and Oxidation Reactivity, Energy & Fuels 31 (2017) 6413-6421.
[37] J. Song, M. Alam, A.L. Boehman, U. Kim, Examination of the oxidation behavior of biodiesel soot, Combustion and Flame 146 (2006) 589-604.
[38] F. Emmerich, Evolution with heat treatment of crystallinity in carbons, Carbon 33 (1995) 1709-1715.
[39] H. Marsh, K. Kuo, Kinetics and catalysis of carbon gasification, Introduction to carbon science, Elsevier1989, pp. 107-151.
[40] R.L. Vander Wal, C.J. Mueller, Initial Investigation of Effects of Fuel Oxygenation on Nanostructure of Soot from a Direct-Injection Diesel Engine, Energy & Fuels 20 (2006) 2364-2369.
[41] R.L. Vander Wal, A.J. Tomasek, Soot nanostructure: dependence upon synthesis conditions, Combustion and Flame 136 (2004) 129-140.
[42] J. Wei, C. Song, G. Lv, J. Song, L. Wang, H. Pang, A comparative study of the physical properties of in-cylinder soot generated from the combustion of n -heptane and toluene/ n -heptane in a diesel engine, Proceedings of the Combustion Institute 35 (2015) 1939-1946.
[43] K. Yehliu, R.L. Vander Wal, O. Armas, A.L. Boehman, Impact of fuel formulation on the nanostructure and reactivity of diesel soot, Combustion and Flame 159 (2012) 3597-3606.
[44] J.D. Levinthal, Investigation of soot oxidation kinetics, nanostructure and surface elemental analysis, Master thesis, The University of Utah, (2013).
[45] C.K. Gaddam, R.L. Vander Wal, X. Chen, A. Yezerets, K. Kamasamudram, Reconciliation of carbon oxidation rates and activation energies based on changing nanostructure, Carbon 98 (2016) 545-556.
[46] G.D.G. Peña, M.M. Alrefaai, S.Y. Yang, A. Raj, J.L. Brito, S. Stephen, T. Anjana, V. Pillai, A. Al Shoaibi, S.H. Chung, Effects of methyl group on aromatic hydrocarbons on the nanostructures and oxidative reactivity of combustion-generated soot, Combustion and Flame 172 (2016) 1-12.
[47] G.D.G. Peña, A. Raj, S. Stephen, T. Anjana, Y.A.S. Hammid, J.L. Brito, A. Al Shoaibi, Physicochemical properties of soot generated from toluene diffusion flames: Effects of fuel flow rate, Combustion and Flame 178 (2017) 286-296.

[48] A. Sharma, T. Kyotani, A. Tomita, Comparison of structural parameters of PF carbon from XRD and HRTEM techniques, Carbon 38 (2000) 1977-1984.
[49] R.L. Vander Wal, V.M. Bryg, M.D. Hays, XPS analysis of combustion aerosols for chemical composition, surface chemistry, and carbon chemical state, Analytical Chemistry 83 (2011) 1924-1930.
[50] M. Pumera, H. Iwai, Multicomponent metallic impurities and their influence upon the electrochemistry of carbon nanotubes, The Journal of Physical Chemistry C 113 (2009) 4401-4405.
[51] C.K. Gaddam, R.L. Vander Wal, Physical and chemical characterization of SIDI engine particulates, Combustion and Flame 160 (2013) 2517-2528.
[52] H. Estrade-Szwarckopf, XPS photoemission in carbonaceous materials: A "defect" peak beside the graphitic asymmetric peak, Carbon 42 (2004) 1713-1721.
[53] I.C. Jaramillo, C.K. Gaddam, R.L. Vander Wal, C.-H. Huang, J.D. Levinthal, J.S. Lighty, Soot oxidation kinetics under pressurized conditions, Combustion and Flame 161 (2014) 2951-2965.
[54] R.L. Vander Wal, A. Yezerets, N.W. Currier, D.H. Kim, C.M. Wang, HRTEM Study of diesel soot collected from diesel particulate filters, Carbon 45 (2007) 70-77.
[55] J. Dahn, W. Xing, Y. Gao, The "falling cards model" for the structure of microporous carbons, Carbon 35 (1997) 825-830.